Optical Vivaldi Antenna Array for Solar Energy Harvesting

W. Amara[1], J. Rouabeh[2], R. Ghayoula[3], A. Hammami[4], A. Smida[5], I. El Gmati[6] and A. Ferchichi[7]

[1]SysCom Laboratory, ENIT, University of Tunis El Manar, Tunis 1068, Tunisia
[2]Department of Technology, Faculty of Science, Gafsa, Tunisia
[3]Faculty of engineering, Moncton University, New Brunswick, Canada
[4]Laboratory (IRESCOMATH), ISSIG, University of Gabes, Tunisia
[5]Department of Medical Equipment Technology, College of Applied Medical Sciences, Majmaah University, Almajmaah 11952, KSA
[6]College of Engineering at Al Gunfudha Umm Al Qura University, KSA
[7]Higher Institute of Applied Sciences and Technology of Mateur, Tunisia

Corresponding author: I. El Gmati (e-mail: iagmati@uqu.edu.sa)

ABSTRACT

In this paper, our objective is to optimize energy harvesting for our application by designing an efficient optical antenna that can capture solar radiation and convert it from AC to DC through the integration of a rectifier. Our approach involves the development of a Vivaldi optical antenna designed to maximize the electric field captured within its gap. Additionally, we explore the utilization of optical arrays (double, four, and eight structures) to enhance the concentration of the captured electric field within a shared gap, as compared to a single antenna structure. To efficiently harness the captured electric field from each individual antenna's gap, we employ feeding lines leading to a common gap.

These innovative systems represent compact electronic devices typically comprising a low-power computer, wireless sensors, and an antenna, enabling communication with their surrounding environment. However, these devices are equipped with on-board energy sources in the form of cells or batteries that necessitate periodic maintenance, such as replacement or recharging. These maintenance requirements can impede the mobility and widespread deployment of these communication systems. Consequently, there is a growing interest in advancing energy autonomy and achieving complete independence from on-board power sources for these systems.

INDEX TERMS Solar Energy, Optical Vivaldi, Antenna Array, radiation pattern

I. INTRODUCTION

Solar energy harvesting represents a pivotal frontier in the global quest for sustainable and renewable energy sources. As the world grapples with the pressing need to mitigate climate change and transition towards cleaner energy alternatives, harnessing the power of the sun has emerged as a beacon of hope. Solar energy, derived from the abundant and virtually inexhaustible supply of sunlight, holds immense promise in meeting our ever-increasing energy demands while reducing our carbon footprint.

The concept of solar energy harvesting revolves around the efficient capture, conversion, and utilization of solar radiation to generate electricity or thermal energy. Unlike conventional fossil fuels, solar energy is clean, renewable, and readily available in most regions of the world. It provides a viable solution to reduce our reliance on finite and environmentally harmful energy sources. The key to unlocking the potential of solar energy lies in the development of cutting-edge technologies and innovative approaches that optimize energy conversion processes. Solar panels, or photovoltaic cells, have long been at the forefront of this endeavor, converting sunlight directly into electricity with remarkable efficiency improvements over the years. However, the pursuit of even more efficient, cost-effective, and versatile methods for solar energy harvesting continues to drive research and innovation in this field. Solar energy has gained significant attention in recent times as a prominent renewable energy source [1]. This energy is harnessed through rectifying antennas that operate in the infrared frequency band [2]. Various design approaches have been explored for this application, including rectangular [3]- [4]circular, spiral, bowtie [5] [6] [7] [8], dipole [9] [10] [11], elliptical [12], and Vivaldi antennas [13].

Optical antennas are now widely employed across diverse fields, including medical applications such as cancer treatment [14]. In cancer treatment, optical antennas are placed in contact with malignant breast tissue containing cancerous tumors. They are then stimulated by near-infrared waves, resulting in localized temperature elevation to destroy cancer cells. Furthermore, these antennas serve as sensors in biology [15], with a focus on monitoring the plasmon resonance shift

in particles based on the species being studied. Moreover, optical antennas find applications in photonics and photovoltaic cells [16]for electricity generation.

An optical Rectenna combines an infrared-receiving antenna with a rectifying diode, unlike photovoltaic cells, which are limited by semiconductor bandgaps in terms of conversion efficiency. Rectennas utilize the inherent nature of light waves, achieving conversion efficiencies as high as 100% [7]. To realize this application successfully, it requires high-quality antenna materials, efficient infrared reception, and precise impedance matching between the rectifier and the antenna [7]. For a specific operating frequency, nano-antennas must be optimized to maximize the enhancement of the electric field intensity.

This study primarily focuses on enhancing the captured field in proximity to the antenna. Initially, we aim to optimize a single Vivaldi nano-antenna to achieve the maximum electric field capture across its gap. Subsequently, we design arrays with two, four, and eight antennas, all sharing a common gap within each array. Feeding lines are employed to gather the near electric field from each structure. The objective is to identify the configuration that offers the highest field capture across the gap [18].

Tables 1, 2, and 3 provide a comparative analysis of Optical Vivaldi Antenna Arrays for solar energy harvesting, including key parameters such as efficiency, frequency range, dimensions, material, installation, and cost. You can customize the values based on your actual research data.

Using this table, you can compare substrates based on their characteristics to determine which one is best suited for your specific antenna application. For example, if you require low loss tangent to reduce energy dissipation, you may choose a substrate with a lower loss tangent. Similarly, if you need a wide frequency range, you can select a substrate suitable for that range.

The structure of this paper is as follows: Section 1 presents the mathematical formulation and antenna design geometry. Section 2 elaborates on the simulation results and interpretations for the single Vivaldi antenna. Section 3 provides an overview of the total field within an array and its corresponding geometry. It also includes CST simulation results for the various array configurations considered. Finally, in Section 4, we offer some concluding remarks.

II. SINGLE VIVALDU ANTENNA DESIGN

The vivaldi nano-antenna presented in Figure 1 was designed for solar energy collection. It has been considered as a good resonators in a large bandwidth . This antenna is effectively used in array conception and development thanks to its miniature size. To design the vivaldi nano-antenna, we considered the following equations:

$$g(x) = B\left(e^{Vx} - e^{V-x}\right) + \frac{w_{min}}{2} \tag{1}$$

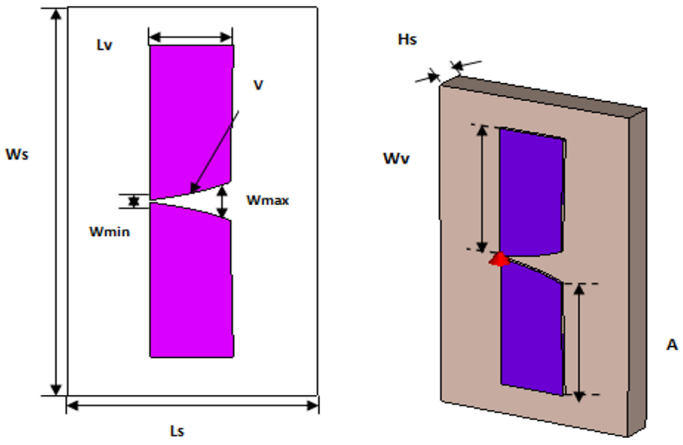

FIGURE 1. Antenna design

Where the constant B is given by

$$B = \frac{\frac{w_{max}}{2} - \frac{w_{min}}{2}}{e^{VL_v} - e^{-V}} \tag{2}$$

w_{max} is the maximum width of the tapered slot, w_{min} corresponds to the minimum width of the tapered slot, V represents the curvature coefficient and L_v denotes the length of the antenna. The first design, printed on a GaAz substrate, contains a single gold vivaldi antenna of thickness $h_v = 0.12um$ and a gap size of $0.05um$.The geometrical parameters of this structure are : $w_s = 6um$, $L_s = 10um$, $H_s = 1um$, $L_v = 2um$, $w_v = 4um$, $A = 3.553$, $w_{min} = 0.05$, $w_{min} = 0.984$ and $V = 0.8um$.

A. COMPLEX PERMITTIVITY MODEL

At radio frequency, metal is considered as a perfect electric conductor, which is not the case at infrared frequency because its dielectric properties usually change with frequencies [17].

The complex dielectric function ε_c is as follows:

$$\varepsilon_c = \varepsilon_1 + i\varepsilon_2 \tag{3}$$

The Drude model dielectric function is presented by the equation below:

$$\varepsilon_c = \varepsilon_\infty - \frac{w_{p1}^2}{w^2 - i\Gamma w} + \frac{w_{p2}^2}{w_0^2 - w^2 + i\gamma w} \tag{4}$$

ε_c symbolizes the finite material conductivity where i is the imaginary unit,ε_∞ stands for the contribution of the bound electron to the permittivity, γ denotes the damping frequency,w_p is the plasma frequency, w represents the angular frequency and w_0 corresponds to the angular frequency.
For this structure, we used the gold as the conductor at the infrared frequencies in the optical and near infrared regions. The constants of (4) are:
$w_0 = \frac{2\pi c}{\lambda_0}$,$\lambda_0 = 450nm$, $\varepsilon_\infty = 8$, $w_{p1} = 13.8 \times 1015s^{-1}$, $w_{p2} = 45 \times 1014s^{-1}$, $\Gamma = 1.075 \times 1014s^{-1}$, $\gamma = 9 \times 1014s^{-1}$.

Antenna Type	Substrate	Frequency Range	Gain	Efficiency	Beamwidth	Dimensions	Polarization	Directivity
Vivaldi A	FR4	2 - 10 GHz	8.5 dBi	70%	60 degrees	100x20 mm	Linear	12 dB
Vivaldi B	Rogers RT/Duroid	1 - 8 GHz	9.2 dBi	80%	50 degrees	120x120 mm	Circular	13 dB
Vivaldi C	Teflon	3 - 12 GHz	10.8 dBi	75%	45 degrees	80x80 mm	Linear	11.5 dB

TABLE 1. Comparison of Antipodal Vivaldi Antennas with Different Substrate Materials

Antenna Type	Efficiency (%)	Frequency Range (THz)	Dimensions (mm)	Material	Installation
Optical Vivaldi A	65	0.5 - 2	10 x 5	Silicon	Rooftop
Optical Vivaldi B	72	0.2 - 1.5	15 x 15	Gold	Ground-mounted
Optical Vivaldi C	68	1 - 4	8 x 8	Aluminum	Building-integrated
Optical Vivaldi D	70	0.8 - 3	12 x 6	Dielectric	Facade-mounted

TABLE 2. Comparative Table for Optical Vivaldi Antenna Array in Solar Energy Harvesting

Ref.	**Substrate**	**Permittivity**	**Loss Tangent**	**Thickness**	**Size (mm^2)**	**Return Loss (dB)**	**Gain (dB)**	**Frequency (GHz)**	**Applications**
[20]	FR-4	4.4	0.02	1.6	80 x 60	-30	2-8	3.1-10.6	UWB
[21]	F4BM265	2.65	0.001	1	130 x 80	-27	2.27-14	1.13-12	UWB
[22]	RO3006	6.15	0.002	1.28	45 x 60	-30	2.2-6.8	1.7-11	UWB
[23]	RO5880	2.2	0.009	0.508	171 x 202	-42	4-8.5	0.67-6	Construction
[24]	RO4003	3.38	0.0027	0.508	40 x 60	-50	8-15	3.4-40	µWave
[25]	RO3006	6.15	0.002	1	39.4 x 34.6	-40	-2-5.2	3.1-10.6	UWB
	FR-4	4.4	0.02	1.4	40.16 x 42.56	-28	-1-5	3.1-10.6	

TABLE 3. Comparison of Substrates for Antenna Applications

Antenna Type	**Frequency Range (GHz)**	**Gain (dBi)**	**Efficiency (%)**	**Dimensions (mm)**	**Material**	**Application**
Optical Vivaldi (Our Work)	0.3 - 3 THz	15.5	75	100 x 50	Silicon	Solar Energy Harvesting
Infrared Antenna A	0.1 - 1 THz	12.2	68	80 x 40	Germanium	Infrared Sensing
Infrared Antenna B	0.2 - 2 THz	13.8	72	90 x 45	Gallium Arsenide	Infrared Imaging

TABLE 4. Comparison of Antennas at Different Frequencies

Antenna Type	**Frequency Range (GHz)**	**Gain (dBi)**	**Efficiency (%)**	**Dimensions (mm)**	**Material**	**Application**
Optical Vivaldi (Our Work)	0.3 - 3 THz	15.5	75	100 x 50	Silicon	Solar Energy Harvesting
Infrared Antenna A	0.1 - 1 THz	12.2	68	80 x 40	Germanium	Infrared Sensing
Infrared Antenna B	0.2 - 2 THz	13.8	72	90 x 45	Gallium Arsenide	Infrared Imaging
Microwave Antenna X	2 - 18 GHz	18.9	82	120 x 60	Copper	Radar
Millimeter-wave Antenna Y	30 - 300 GHz	22.3	88	60 x 30	Aluminum	5G Communication

TABLE 5. Comparison of Antennas at Different Frequencies

Ref. no	**Frequency bands (THz)**	**Dimensions (μm^2)**	**Type of antenna**	**Gain (dBi)**	**Efficiency (%)**
Our Work	5-30 THz	6×10	Optical vivaldi antenna	2.23	75.5
[27]	0.33–0.37	600×600	Quarter wave transformer	6.3	74.5
[28]	0.19–0.24, 0.57–0.59	850×770	Dual-band Z-shaped circularly polarized	5.08	-
[29]	0.6, 0.8	500×500	Double dielectric THz antenna	10.34	84.50
[30]	0.44–0.71	300×300	Micro-sized rhombus-shaped antenna	5.7	97.3
[31]	0.63	800×600	PBG-based THz antenna	8.6	85.71
[32]	0.5–0.8	1000×1000	EBG-based high-gain THz antenna	15.1	83.7
[33]	1.56	950×950	Multiband THz PBG antenna	10.51	-
[34]	0.5–0.8	600×600	THz antenna based on photonic crystals	9.19	90.84
[35]	0.5–0.7	500×500	THz antenna based on PBG and FSS	8.15	-
[36]	0.7	179×211	Terahertz graphene-based reconfigurable antenna	7.1	-
[37]	0.92–1.2	93×120	Double-ring nanoribbon graphene-based antenna	6.0	44
[38]	0.725–0.775	208.98×433.2	Graphene nanoribbon-based terahertz antenna	5.71	86.58
[39]	0.98–1.06	190×150	Graphene-based antenna	6.82	66.72
[40]	2.15–2.2, 2.56–2.6	100×100	Beam reconfiguration dual-band graphene antenna	7.19	64.12
[41]	1.05–1.14	180×212	Fishnet-based metamaterial loaded antenna	3.57	-
[42]	0.96–0.99	180×212	SRR-based THz antenna	5.75	-
[43]	0.69	210×180	THz antenna based on PBG and FSS	6.79	-

TABLE 6. Comparison of THz Antennas

TABLE 7. Optimized parameters of the Vivaldi nano-antenna.

Parameter	Value (µm)
Substrate width, W	10
Substrate thickness h	1
Maximum width of the tapered slot w_{max}	0.948
Minimum width of the tapered slot w_{min}	0.05
Curvature coefficient C	0.8

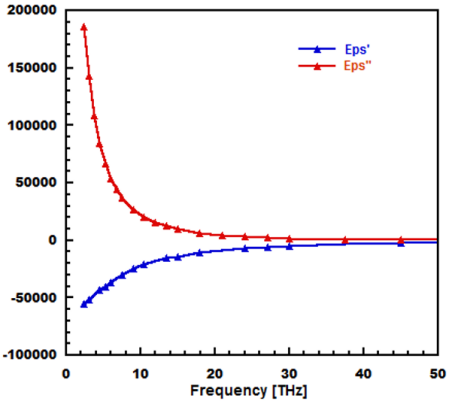

FIGURE 2. Variation of the real and imaginary parts of gold permittivity

This complex expression of the permittivity affords a dielectric function which approaches the experimentally-mesured dielectric functions by johnson and christy for gold [17] [18]. This function was a great approximation particularly for wavelengths greater than 500 nm.

B. SIMULATION RESULTS OF THE SINGLE VIVALDI ANTENNA

The calculated results are reflexion coefficient,bandwidth, radiation pattern of gain and directivity, electric near field. CST microwave studio calculated some of these results.

1) S parameter

Figure 3 illustrates the return loss of the nano-antenna. Examining this graph, we observe effective impedance matching ($|S_{11}| < -10dB$) within the frequency range spanning from 5 to 30 THz. The highest return loss value occurs at 10.72 THz, measuring -25.67 dBi. Unlike conventional antennas such as dipoles, as depicted in Figure 2, this antenna does not exhibit a single resonance. Instead, it displays a dual-resonance behavior across the entire THz frequency spectrum under consideration.

Indeed, relying solely on the S parameter proves inadequate for a comprehensive characterization and evaluation of antenna performance. As an alternative approach, it is feasible to augment the assessment by including additional metrics such as simulated radiation efficiency, gain as a function of frequency, or the simulated input impedance of the port excitation, among others.

2) Simulated radiation efficiency and gain

From Figure 4(a), we observe two distinct trends in the variation of radiation efficiency. Initially, it exhibited an increase,

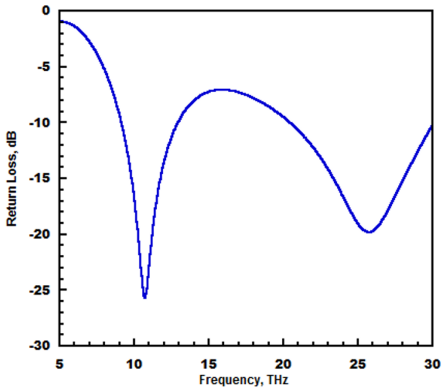

FIGURE 3. Simulated antenna return loss versus the frequency [5..30THz]

reaching up to 75% at 15 THz. Subsequently, there was a decline, bringing it down to 50% at 30 THz. Notably, the radiation efficiency surpassed the 50% threshold within the frequency range spanning from 10 to 15 THz. It's important to highlight that this efficiency decreased to 50% at 29 THz, primarily due to the losses incurred by metals at infrared frequencies.

The trend in gain was notably evident in Figure 4(b), where it showcased an increase with frequency over a substantial frequency band. The maximum gain was consistently observed within the range of 15 to 30 THz.

3) Input impedance

As depicted in Figure 5, it is evident that the real component of the input impedance, which can be distinctly identified as the input resistance, remained relatively constant at around 100Ω. Furthermore, the imaginary component (input reactance) exhibited oscillations that approached zero within the frequency range spanning from 5 to 30 THz.

4) Far field (Gain + Directivity) at 12.4 THz

In Figure 6, we showcase the three-dimensional radiation pattern, depicting both the directivity and gain at the frequency of 12.4 THz. The outcomes of this analysis reveal that the directivity value stands at 2.23 dBi.

Additionally, it's noteworthy that the radiation pattern of antenna gain exhibited omnidirectional characteristics at the frequency of f=12.4 THz, accompanied by a simulated low gain of approximately 0.37 dB.

5) The effect of incident plane wave polarization

The antenna received illumination from a linearly polarized plane wave with an electric field intensity of 1 V/m. This plane wave excitation can be mathematically represented by the following equation:

$$S_y(y) = E_0 e^{(-j\beta_0 y)} \tag{5}$$

In the scenario described, the incident electric field aligns with the Vivaldi antenna's axis (along the y-axis), while the direction of propagation is perpendicular to the antenna

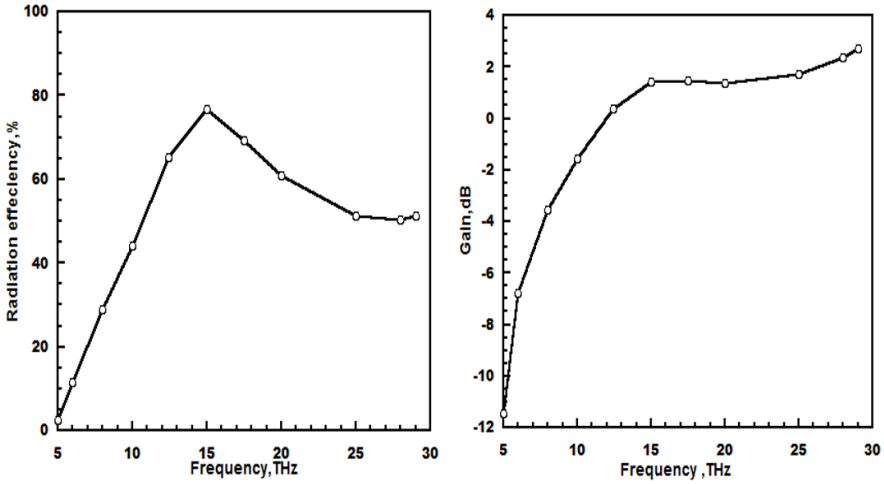

(a) (b)

FIGURE 4. Simulated (a): radiation efficiency, (b): gain over frequency band [5...30THz]

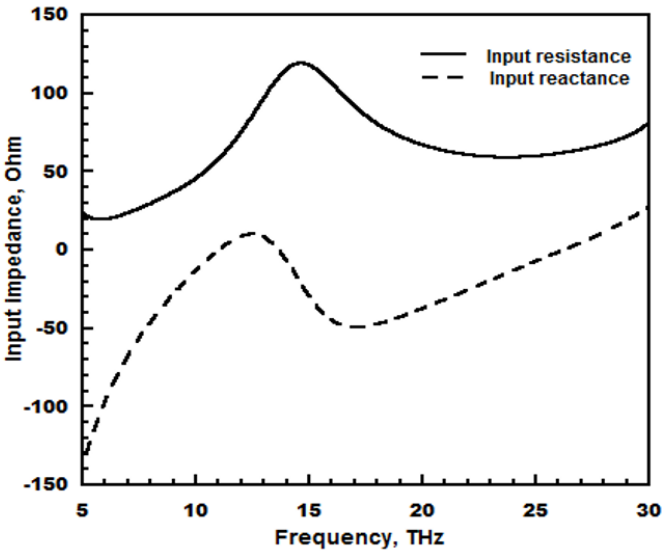

FIGURE 5. The Simulated input resistance and reactance of the Vivaldi antenna

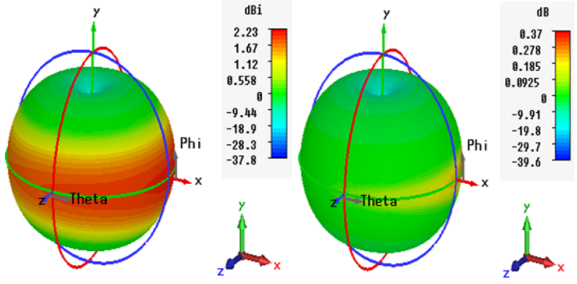

FIGURE 6. 3-D Radiation pattern of directivity and gain at 12.4 THz

(along the negative z-axis). Based on Maxwell's equations and subsequent mathematical derivations and simplifications [19], we obtain the following expressions:

$$\nabla \times \left(\mu^{-1} \nabla \times E\right) - \beta_0^2 E \left(\varepsilon_r - j\frac{\sigma}{\omega}\right) = 0 \qquad (6)$$

where $\beta_0 = w\sqrt{\varepsilon_0 \mu_0}$, $\varepsilon_0 = 8.854 \times 10^{-12} Fm^{-1}$ is the permittivity in free space and $\mu_0 = 4\pi 10^{-7} Hm^{-1}$ is the permeability.

For dipole antenna the electric field of each antenna at surface (XY plane), we need just $\mathrm{E}_z^s written as follows$:

$$E_z^s = -j\frac{1}{\omega\mu\varepsilon}\left(\beta_0^2 + \frac{\partial A_z}{\partial Z^2}\right) \qquad (7)$$

Where A_z is the potential vector.

Indeed, the optimized antenna dimension and geometry made the collection of the solar energy at the infrared frequency possible. This structure was simulated in order to study the electric field enhancement in its gap.

Figure 7 presents the distribution of the electric field within the near-infrared region, specifically within the frequency band spanning from 5 to 30 THz. As previously demonstrated in our findings (Figure 7 and Figure 8a), the maximum electric field was observed at 12.4 THz, measuring 83.1 V/m. Notably, in our case, the significant electric field value was concentrated within the gap, setting it apart from isolated particles. It was evident that the most substantial electric field strength was localized at this gap.

The concentration of the captured electric field within the nano-gap was contingent upon several geometric parameters, including the size of the Vivaldi antenna, the dimensions of the gap, the substrate thickness, the thickness of the gold Vivaldi, and the length of the feeding line.

Figure 8 illustrates the impact of substrate thickness on the electric field intensity captured at the gap. It is evident that the substrate thickness played a crucial role in influencing the electric field collected by the antenna. Altering this parameter

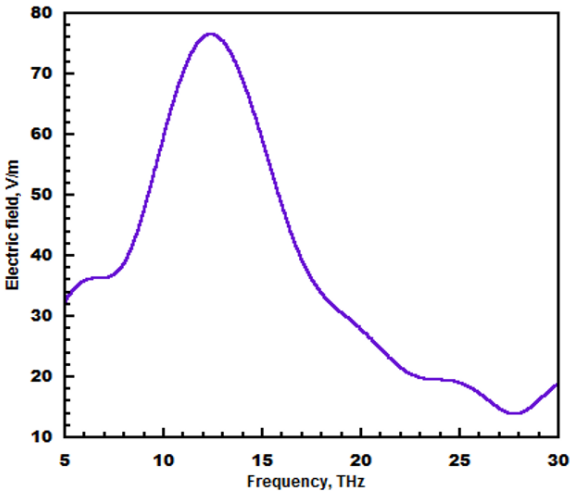

FIGURE 7. Electric field distribution for single antenna

resulted in variations in the antenna's performance. Specifically, as the substrate thickness increased, the maximum electric field concentration at the antenna's tip also increased. When examining the field variation across the frequency band spanning from 5 THz to 30 THz, it reached its peak at 11.9 THz for a substrate thickness of $2\mu m$, with a maximum recorded value of 78.372 V/m.
Furthermore, the optimized Vivaldi antenna was analyzed and studied for different thicknesses of gold layer. We varied the thickness of gold layer by a step of 0.02 μm in order to obtain the greatest field improvement.

Looking at Figure 8(b), it becomes evident that when the thickness is reduced, the field experiences a significant enhancement. The peak field intensity is prominently observed at 13.32 THz for a thickness of 0.08 μm, measuring at 89.214 THz. It can be inferred that as the gold thickness decreases, the field intensity captured within the gap also increases.
The following table summarizes the maximum field, obtained for different thicknesses of substrate and for a fixed gold layer thickness value equal to 0.12 μm, as well as the maximum field for various thicknesses of gold layer and for a fixed substrate thickness of 1 μm for the optimized Vivaldi antenna.

6) Single Vivaldi antenna coupled with a feeding line

In the subsequent investigation, the Vivaldi antenna was integrated with a feeding line positioned at the structure's center. This arrangement involved the elimination of the gap, and the electric field was subsequently computed at the termination point of the feeding line.

The additional feeding line, depicted in Figure 9b, possessed specific dimensions with a width of 0.3 m and a length of 3.975 m. What's intriguing to observe is that the conjunction of the antenna with the feeding line resulted in a notably weaker electric field compared to the concentration of the field observed at the gap of the single element. Surprisingly, the presence of the feeding line played a crucial role in mitigating field losses and directing the electric field from all antennas toward a shared gap during the array design process.

III. ANTENNA ARRAY DESIGN AND SIMULATIONS RESULTS

For identical elements in an array, the overall performance could be controlled by several factors such as:
- The arrangement's geometry (whether it's linear, circular, etc.).
- The distance separating its elements.
- The relative pattern of each element.
- The excitation phase and the element amplitude.

The collection of individual antenna elements can be strategically arranged to create a planar array. The cumulative field produced by all the antennas is obtained by adding together the vector contributions from each antenna element's radiated field. In essence, the electric field captured by the antenna array is the summation of all the fields captured by each individual antenna. Therefore, we can determine the overall field generated by the array by multiplying the field produced by each antenna by a factor known as the "array factor" [13]- [17]. The array factor is mathematically expressed as follows:

$$AF = \sum_{m=1}^{M} I_{m1} e^{j(m-1)\psi} \tag{8}$$

Where
$\psi = \beta_0 d cos\phi + \beta$,ψ represents the relative phase between the elements.
$\psi_x = \beta_0 d_x sin\theta cos\phi + \beta_x$, if identical antennas are put along x axis.
$\psi_y = \beta_0 d_y sin\theta cos\phi + \beta_y$, if identical antennas are put along y axis.

I_{m1} represents the excitation coefficient of a single element antenna of an array, d is the distance separating two elements in an array and β corresponds to the phase shift between elements.
When K is the number of element as an array put along the particular y-axis, the expression of the array factor becomes:

$$\sum_{k=1}^{K} I_{k1} \left(\sum_{m=1}^{M} I_{m1} e^{j(m-1)\psi_x} \right) e^{j(k-1)\psi_y} \tag{9}$$

The most practical and simplest arrays was composed of several elements placed along a line. We started by using two-element array.

A. DUAL VIVALDI

In the second design, as depicted in Figure 10, we introduced a pair of Vivaldi antennas interconnected by a shared feeding line. This arrangement was situated on the same dielectric

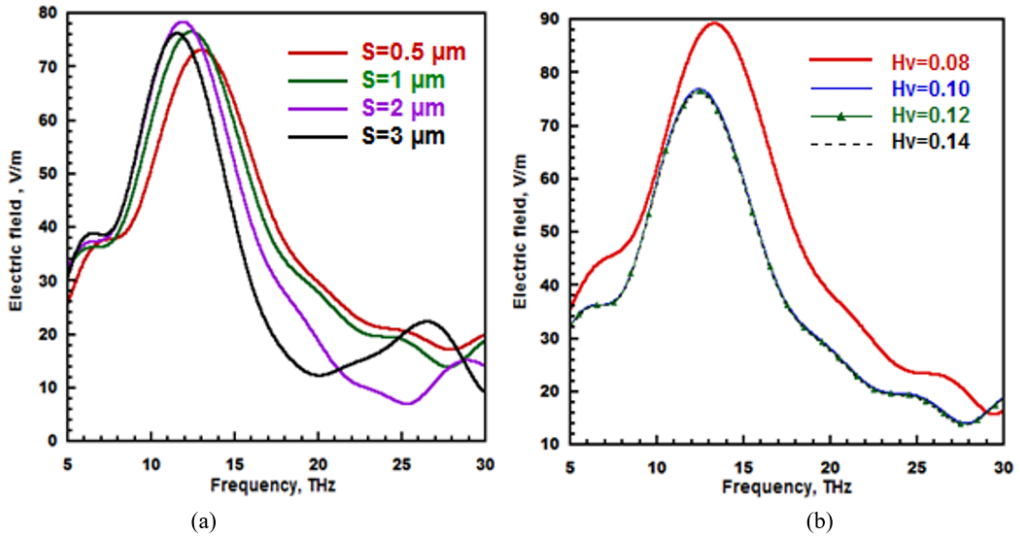

(a) (b)

FIGURE 8. Electric field distribution versus frequency for selected, (a): gold layer thickness, (b): substrate thickness

TABLE 8. Max E-field for selected old layer and substrate thickness

Substrate thickness (μm)	Max E-field (V/m)	Gold layer thickness (μm)	Max E-field (V/m)
0.5	73.128	0.08	89.214
1	76.527	0.10	76.996
2	78.372	0.12	76.527
3	76.238	0.14	76.122

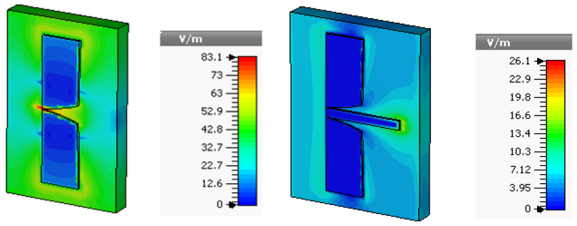

(a) (b)

FIGURE 9. Electric field distribution for the single nano-antenna at 12.4 THz with and without feeding line

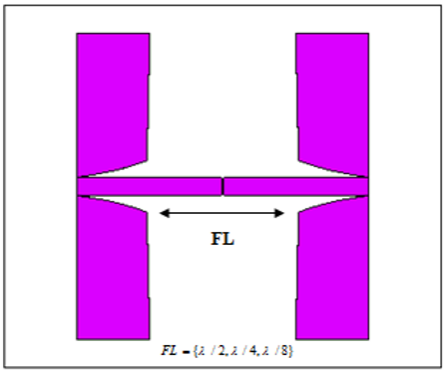

FIGURE 10. Double antenna connected with feeding line

substrate as the single antenna, with dimensions measuring 12µm×10µm. The primary objective was to enhance the maximum captured electric field value, as illustrated in Figure 8. To achieve this, feeding lines were utilized to convey the electric field captured within the gap of each individual antenna towards a common gap.

To optimize the captured electric field value and attain optimal results, we made adjustments to both the length and width of the feeding line. Additionally, the spacing between the antenna elements proved to be a significant factor in influencing the intensity of the captured electric field, a relationship elucidated in the subsequent results presented in Figures 10 and 11.

As depicted in Figure 11, the substrate had specific dimensions. It was evident that the length of the feed line (FL) positioned between the two structures played a decisive role in augmenting the electric field. This analysis was carried out for an antenna designed for a 50Ω configuration, with a microstrip width of 500 nm. According to the outcomes of numerical simulations, when FL was configured at $\lambda/8$, the electric field attained its zenith, registering at 103 V/m at 10.52 THz. Conversely, when FL was adjusted to $\lambda/4$, the peak electric field was observed at 196 V/m and occurred at 7.65 THz. In the quest to optimize the electric field intensity of the optical double element, refinements were made to the dimensions of the feeding line. Ultimately, the most favorable outcome materialized when FL was set at $\lambda/2$, yielding a maximum electric field value of 300 V/m at 5 THz.

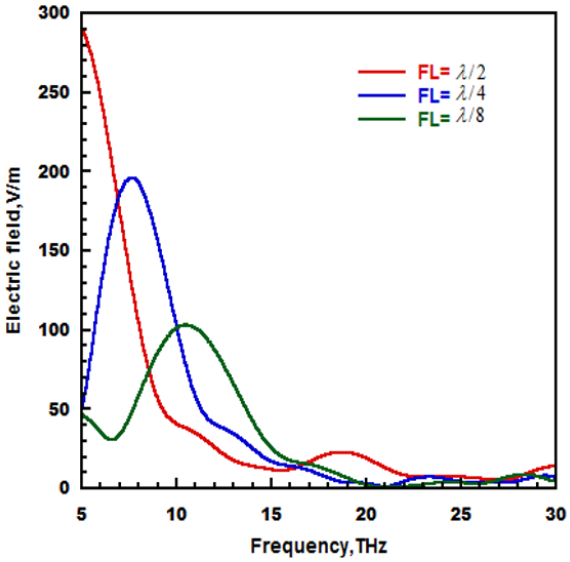

FIGURE 11. Electric field distribution with different feeding line lengths FL

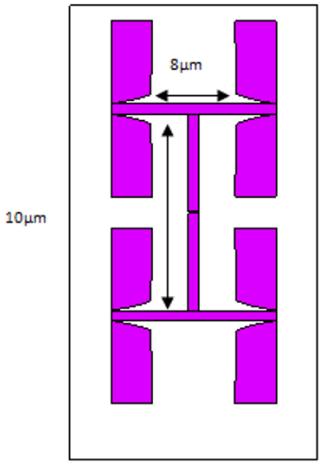

FIGURE 12. Vivaldi nano-array configuration with four antennas

B. OPTICAL ARRAY WITH FOUR ANTENNAS

A 2×2 Vivaldi nano-array was designed to enhance the captured electric field, as presented in Figure 12. The size of the substrate was $12\mu m \times 22\mu m$ with thickness of $1\mu m$. It was constructed by four antennas connected by a feeding line to facilitate the collection of the field from the array element with a common gap. Vivaldi arrays have been studied and utilized because of their wide band and their high performance.

This optical array with 4 antennas offered the highest electric field, compared to a single antenna. The maximum value of the field occurred at 343.479 V/m at 5 THz, as shown in Figure 13. The captured field was concentrated inside the gap with maximum value of 450 V/m at 5 THz, as presented in Figure 14.

In Figure 15, we compare these different configurations of capacities to harvest the solar energy. It was clear that the array with four antennas had the greatly value of the captured field, compared to the double structure and the single design.

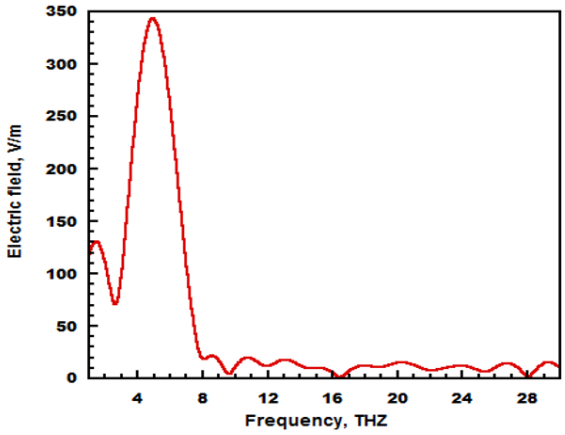

FIGURE 13. Electric field distribution versus frequency for the optical array

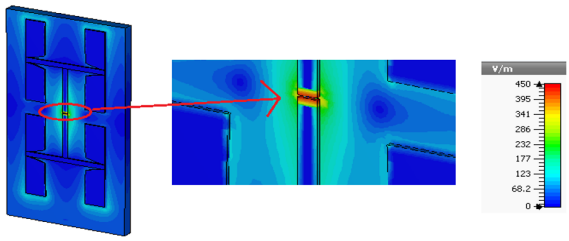

FIGURE 14. Electric field distribution at 5 THz for four antennas

C. OPTICAL ARRAY WITH EIGHT ANTENNAS

1) Configuration 1:

The spacing between the two arrays of four antennas was fine-tuned to 20.3 μm, excluding the 50 nm slot. This two-array antenna configuration was positioned onto a GaAs substrate measuring 32.6 μm in width, 22 μm in length, and having a thickness of 1 μm. You can refer to the visual representation of this design in Figure 15a.

2) Configuration 2:

For the second configuration(Figure 15 b) , the length of the connecting feeding lines for parallel configuration was set to 8.3 μm. The optimized length between the two arrays of four antennas was $20.3\mu m$ without considering the slot of 50 nm. It was printed on a dielectric substrate with size of 16 μm $\times 40\mu m$. It can be perfectly seen that the nano-gap size at the feeding point was fixed for all the studied configurations and structures. This size corresponded to 50 nm for different cases presented in this work.

From the above results (Figures 16 and 17) it can be concluded that the largest field was obtained for the first configuration, the maximum value corresponds to 790 V/m at 2.85 THz. For the second configuration, the maximum field reaches 429 V/m at 1.98 THz. Then we can conclude that the configuration and the location of the antennas affect the captured field and can create the difference and the improvement. It was clear that the captured electric field is concentrated inside the gap compared to the single antenna with a field more propagated around the antenna.

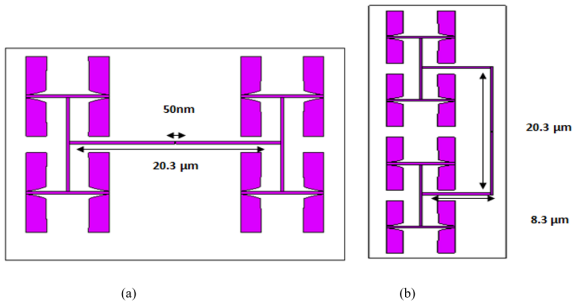

FIGURE 15. Vivaldi optical array with 8 antennas: (a) configuration 1, (b) configuration 2

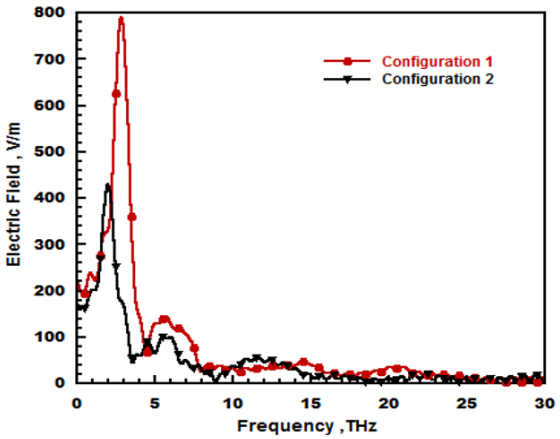

FIGURE 16. Electric field distribution for an array with 8 antennas with two configurations

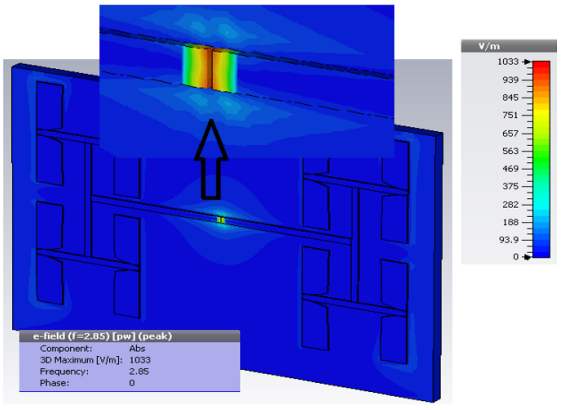

FIGURE 17. Electric field distribution for an array with 8 antennas (configuration 1)

To enhance the electric field captured within the feeding gap, we initially integrated the basic antenna with an optimized transmission line. Subsequently, we augmented the quantity of antenna elements. This strategy proved to be highly effective in augmenting the field strength and necessitated adjustments to various parameters to attain optimal outcomes. Clearly, the quantity of antennas played a pivotal role in elevating the amplitude and values of the electric

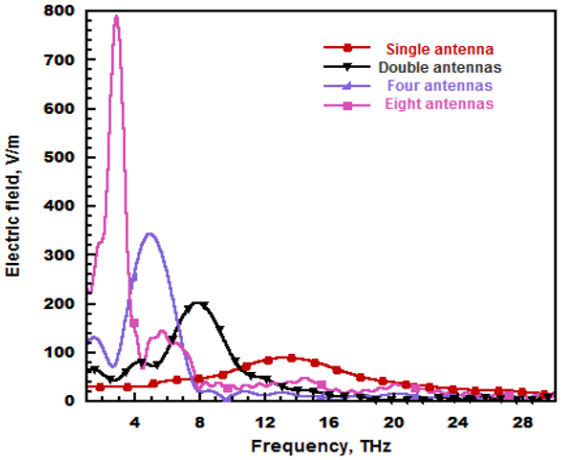

FIGURE 18. Electric field distribution for (single, two, four and eight antennas) over versus Frequency

TABLE 9. The comparison between Vivaldi optical antennas configurations

	Resonant frequency(THz)	Max E-field (V/m)
Single Vivaldi	13.32	89.214
Double Vivaldi	7.884	202.311
Four antennas	4.944	343.479
Eight antennas	2.85	790

field. Within this investigation, each antenna contributed to the electric field collection through a dedicated feeding line. Figure 18 offers a comparative analysis of electric field variations among single, double, four, and eight-element configurations. Notably, these elements exhibited distinct resonance frequencies owing to variations in their configurations and the number of elements employed. The following table provides a comprehensive summary and comparison of the diverse configurations of Vivaldi optical antennas.

It is obvious that the resonance frequency band was constantly changing and shifting with the increase in the number of antennas element in the array. It influenced the frequency resonance and the performance of the array.

IV. CONCLUSION

In this study, we introduced an ultra-wideband optical Vivaldi antenna prototype designed to operate in the infrared region for solar energy collection. Our primary goal was to optimize the collection of electromagnetic radiation, initially utilizing a single antenna and subsequently exploring configurations with two, four, and eight elements of the optical Vivaldi antenna. Our research findings underscore that the maximum value of the electric field captured in the gap between antenna elements depends on several critical parameters. These parameters include the number of elements within an antenna array, the dimensions of the coupling elements, and the distances between individual elements. It is noteworthy that our investigation reveals that the Vivaldi antenna array we examined exhibited remarkable efficiency in capturing the highest electric field values. Furthermore, we conducted an in-depth comparative analysis of the various antenna

configurations to identify the optimized setup that yields the most favorable field values. These field values are pivotal for subsequent conversion into direct current (DC) voltage through the integration of an embedded rectifier. Our findings provide significant insights into the critical factors and essential configurations essential for the successful collection and conversion of solar energy using optical Vivaldi antennas.

ACKNOWLEDGMENT

The authors would like to thank the Deanship of scientific Research Northern Border University for supporting this work by Grant code (23UQU4361156DSR05)

ABBREVIATIONS

DC Direct Current
AC Alternative Current
FL Feed Line

REFERENCES

[1] G. Moddel and S. Grover, "Rectenna Solar Cells" Ed. Springer, New York, 2013.
[2] A. M. A. Sabaawi, C. Tsimenidis, Bayan S. Sharif," Infra-red Nano-antennas for solar energy collection", Loughborough, UK , 14-15 November 2011.
[3] A. M. A. Sabaawi, C. Tsimenidis, Bayan S. Sharif," Infra-red Spiral Nano-antennas", Loughborough, UK , 12-13 November 2012.
[4] G. Jayaswal , A. Belkadi , A. Meredov , B. Pelz , G. Moddel , A. Shamim ," Optical rectification through an Al2O3 based MIM passive rectenna at 28.3 THz", Materials Today Energy 7 (2018) 1-9.
[5] A. Haque, A. Reza, N. Kumar, H. Ramiah, "Slotting Effect in Designing Circular Edge Bow-Tie Nano Antenna for Energy Harvesting", 2015 IEEE Conference on Open System(ICOS), August Melaka, Malaysia.
[6] Gadalla, M. N., M. Abdel-Rahman, and Atif Shamim, "Design, optimization and fabrication of a 28.3 THz nanorectenna for infrared detection and rectification." Scientific reports 4, 2014.
[7] M. A. Sabaawi, C. Charalampos, Tsimenidis, and S. Sharif, "Planar Bowtie Nanoarray for THz Energy Detection", IEEE Transactions on Terahertz Science and Technology, Vol. 3, No. 5, September 2013.
[8] Islam E. Hashem, Nadia H. Rafat, and Ezzeldin A. Soliman, "Dipole Nantennas Terminated by Traveling Wave Rectifiers for Ambient Thermal Energy Harvesting", IEEE Transactions On Nanotechnology, VOL. 13, NO. 4, JULY 2014.
[9] N. A. Eltresy, H. A. Malha, S. H. Zainud-Deen, and K. H. Awadalla, Dual-Polarized Nanoantenna Solar Energy Collector, 33rd National radio science conference (NRSC 2016), Aswan, Egypt, Feb 2225, 2016.
[10] W. Amara, D. Ouleslati, H.Rmili, A. AlGhamdi and T.Aguili, "Numerical Analysis of a Modified-Dipole Optical Antenna for Solar Energy Harvesting",The 2018 International Conference on Innovative trends in Energy (ITE'18), May 10-12, Hammamet-Tunisia.
[11] W. AMARA, D. OUESLATI, H.RMILI, A. ALGHAMDI and T.AGUILI, "Ultra-Wideband Elliptical-Dipole OpticalAntenna for Solar Energy Harvesting", The 2018 International Conference on Sensors, Systems, Signals and advanced technologies, (SSS'18), May 10-12, Hammamet-Tunisia.
[12] W. Amara, N. Elresty, A. Yahyaoui, H. Rmili, T. Aguili, and J. M. Floch, "Design of ultra-wideband nano-antennas for Solar Energy Harvesting"' the Loughborough Antennas and Propagation Conference, LAPC, November 2017.
[13] A. Vial, T. Laroche, and M. Roussey, "Crystalline structure's influence on the near-field optical properties of single plasmonic nanowires," Applied Physics Letters 91, 123101 (2007).
[14] J. Schuller, R. Zia, and M. Brongersma, "Near-field characterization of guided polariton propagation and cutoff in surface plasmon waveguides," Physical Review B 74, 1–12 (2006).
[15] J.-C. Weeber, A.-L. Baudrion, M. Gonzalez, A. Dereux, A. Stepanov, T. Ebbesen , and J. Krenn, E. Devaux, "Design, near-field characterization, and modeling of 45^ A°surface-plasmon Bragg mirrors," Physical Review B 73, 19–21 (2006).
[16] Ordal MA,Bell RJ, Alexander Jr RW, Long LL, Querry MR. Optical properties of fourteen metals in the infrared: Al, Co, Cu, Au, Fe, Pb,Mo,Ni,Pd,Pt,Ag,Ti,V, and W. Appl Otp.1985; 24:4493.
[17] M. Moosazadeh, S. Kharkovsky, J. T. Case, and B. Samali, "UWB Antipodal Vivaldi Antenna for Microwave Imaging of Construction Materials and Structures," Microw Opt Technol Lett., vol. 59, no. 6, pp. 1259–1264, 2016.
[18] C. Balanis , "Antenna theory: analysis and design," New Jersey: Wiley; 2005.
[19] DK Kotter, SD Novack, WD Slafer, PJ Pinhero, "Theory and Manufacturing Processes of Solar Nanoantenna Electromagnetic Collectors," Journal of Solar Energy Engineering, Vol. 132, Feb. 2010.
[20] F. Abayaje and P. Febvre, "A customized reduced size Antipodal Vivaldi Antenna used in Wireless Baseband Transmission for short-range communication," AEU - Int J Electron C, vol. 70, no. 12, pp. 1684–1691, 2016.
[21] S. Zhu, H. Liu, P. Wen, L. Du, and J. Zhou, "A Miniaturized and High Gain Double-Slot Vivaldi Antenna Using Wideband Index-Near-Zero Metasurface," IEEE Access, vol. 6, pp. 72 015–72 024, 2018.
[22] J. A. Hong, H J. G. Jeong and Y. J. Y. I.J. Yoon, "Miniaturized antipodal tapered slot antenna with lower frequency band extension characteristic," Microw Opt Technol Lett., pp. 1570–1573, 2014.
[23] Z. Esmati and M. Moosazadeh, "Reflection and transmission of microwaves in reinforced concrete specimens irradiated by modified antipodal Vivaldi antenna," Microw Opt Technol Lett., vol. 60, no. 9, pp. 2113–2121, 2018.
[24] M. Moosazadeh and S. Kharkovsky, "A Compact High-Gain and Frontto-Back Ratio Elliptically Tapered Antipodal Vivaldi Antenna With Trapezoid-Shaped Dielectric Lens," IEEE Antennas Wireless Propag. Lett., vol. 15, pp. 552–555, 2015.
[25] A. Z. Hood, T. Karacolak, and E. Topsakal, "A small antipodal vivaldi antenna for ultrawide-band applications," IEEE Antennas Wireless Propag. Lett., vol. 7, pp. 656–660, 2008.
[26] P. Bosshard, W. Hermann, and E. Hung, R. Hunt, and A. Simon, "An assessment of solar energy conversion technologies and research opportunities," GCEP Energy Assessment Analysis, 2006.
[27] M. El-Nawawy, A. Allam, D. Korzec, "The design of a 0.35 THz microstrip patch antenna on LTCC substrate," Electr Electron Eng. 2011; 1(1):1-4.
[28] S. Ullah, C. Ruan, T. Haq, "Z-shaped dual band circular polarized microstrip antenna for THz communication," In: In 2019 44th International Conference on Infrared, Millimeter, and Terahertz Waves (IRMMW-THz). IEEE; 2019:1-2.
[29] K. Jha, G. Singh , "Dual-band rectangular microstrip patch antenna at terahertz frequency for surveillance system," J Comput Electron. 2010; 9(1): 31-41.
[30] C. Krishna, S. Das, A. Nella, S. Lakrit, B. Madhav, "A micro-sized rhombus-shaped THz antenna for high-speed short-range wireless communication applications," Plasmonics. 2021; 16(6): 2167-77.
[31] R. Kushwaha, P. Karuppanan, L. Malviya, "Design and analysis of novel microstrip patch antenna on photonic crystal in THz," Physica B. 2018; 545: 107-12.
[32] K. Jha, G. Singh, "Analysis and design of enhanced directivity microstrip antenna at terahertz frequency by using electromagnetic bandgap material," Int J Numer Model Electron Netw Dev Fields. 2011; 24(5): 410-24
[33] A. Singh, S. Singh, "A trapezoidal microstrip patch antenna on photonic crystal substrate for high speed THz applications," Photon Nanostruct-Fundament Appl. 2015; 14: 52-62.
[34] A. Hocini, M. Temmar, D. Khedrouche, M. Zamani, "Novel approach for the design and analysis of a terahertz microstrip patch antenna based on photonic crystals," Photon Nanostruct-Fundament Appl. 2019;36:100723.
[35] A. Nejati, R. Sadeghzadeh, F. Geran, "Effect of photonic crystal and frequency selective surface implementation on gain enhancement in the microstrip patch antenna at terahertz frequency," Phys B: Condensed Matter. 2014;449:113-20.
[36] M.K. Azizi, M. Ksiksi, H. Ajlani, A. Gharsallah, "Terahertz graphene-based reconfigurable patch antenna," Progr Electromagn Res Lett. 2017;71:69-76
[37] M. Nickpay, M. Danaie, A. Shahzadi, "Wideband rectangular double-ring nanoribbon graphene-based antenna for terahertz communications," IETE J Res. 2019;2019:1.
[38] S. Anand, D. Kumar, R. Wu, M. Chavali, "Graphene nanoribbon based terahertz antenna on polyimide substrate. Optik. 2014;125(19): 5546-9.

[39] R. Goyal, D. Vishwakarma, "Design of a graphene-based patch antenna on glass substrate for high-speed terahertz communications," Microw Opt Technol Lett. 2018;60(7):1594-600.
[40] S. Mrunalini, A. Manoharan, "Dual-band re-configurable graphene-based patch antenna in terahertz band for wireless network-on-chip applications," IET Microw Antennas Propag. 2017;11(14):2104-8.
[41] Y. Sirmaci, C. Akin, C. Sabah, "Fishnet based metamaterial loaded THz patch antenna," Opt Quant Electron. 2016;48(2):1.
[42] AT. Devapriya, S. Robinson, "Investigation on metamaterial antenna for terahertz applications," J Microw Optoelectron Electromagn Appl. 2019;18:377-89.
[43] S. Ullah, C. Ruan , T. Haq, X. Zhang, "High performance THz patch antenna using photonic band gap and defected ground structure," J Electromagn Waves Appl. 2019;33(15):1943-54.